

See discussions, stats, and author profiles for this publication at: <https://www.researchgate.net/publication/24193323>

Discriminating the Intraerythrocytic Lifecycle Stages of the Malaria Parasite Using Synchrotron FT-IR Microspectroscopy and an Artificial Neural Network

ARTICLE in ANALYTICAL CHEMISTRY · MAY 2009

Impact Factor: 5.64 · DOI: 10.1021/ac802291a · Source: PubMed

CITATIONS

20

READS

61

9 AUTHORS, INCLUDING:



[Grant Webster](#)

Monash University (Australia)

10 PUBLICATIONS 175 CITATIONS

[SEE PROFILE](#)



[Timothy J Egan](#)

University of Cape Town

126 PUBLICATIONS 4,001 CITATIONS

[SEE PROFILE](#)



[Keith R Bambery](#)

Australian Synchrotron

47 PUBLICATIONS 500 CITATIONS

[SEE PROFILE](#)



[Bayden R Wood](#)

Monash University (Australia)

142 PUBLICATIONS 2,834 CITATIONS

[SEE PROFILE](#)

Discriminating the Intraerythrocytic Lifecycle Stages of the Malaria Parasite Using Synchrotron FT-IR Microspectroscopy and an Artificial Neural Network

Grant T. Webster,[†] Katherine A. de Villiers,[‡] Timothy J. Egan,[‡] Samantha Deed,[§] Leann Tilley,[§] Mark J. Tobin,^{||} Keith R. Bambery,[†] Don McNaughton,[†] and Bayden R. Wood*,[†]

Centre for Biospectroscopy and School of Chemistry, Monash University, Clayton, Victoria 3800, Australia, Department of Chemistry, University of Cape Town, Private Bag, Rondebosch 7701, South Africa, Department of Biochemistry and Centre of Excellence for Coherent X-ray Science, La Trobe University, Melbourne, Victoria 3086, Australia, and Australian Synchrotron, 800 Blackburn Road, Clayton, Victoria 3168, Australia

Synchrotron Fourier transform infrared (FT-IR) spectra of fixed single erythrocytes infected with *Plasmodium falciparum* at different stages of the intraerythrocytic cycle are presented for the first time. Bands assigned to the hemozoin moiety at 1712, 1664, and 1209 cm⁻¹ are observed in FT-IR difference spectra between uninfected erythrocytes and infected trophozoites. These bands are also found to be important contributors in separating the trophozoite spectra from the uninfected cell spectra in principal components analysis. All stages of the intraerythrocytic lifecycle of the malarial parasite, including the ring and schizont stage, can be differentiated by visual inspection of the C–H stretching region (3100–2800 cm⁻¹) and by using principal components analysis. Bands at 2922, 2852, and 1738 cm⁻¹ assigned to the $\nu_{\text{asym}}(\text{CH}_2 \text{ acyl chain lipids})$, $\nu_{\text{sym}}(\text{CH}_2 \text{ acyl chain lipids})$, and the ester carbonyl band, respectively, increase as the parasite matures from its early ring stage to the trophozoite and finally to the schizont stage. Training of an artificial neural network showed that excellent automated spectroscopic discrimination between *P. falciparum*-infected cells and the control cells is possible. FT-IR difference spectra indicate a change in the production of unsaturated fatty acids as the parasite matures. The ring stage spectrum shows bands associated with cis unsaturated fatty acids. The schizont stage spectrum displays no evidence of cis bands and suggests an increase in saturated fatty acids. These results demonstrate that different phases of the *P. falciparum* intraerythrocytic life cycle are characterized by different lipid compositions giving rise to distinct spectral profiles in the C–H stretching region. This insight paves the way for an automated infrared-based technology capable of diagnosing malaria at all intraerythrocytic stages of the parasite's life cycle.

Malaria is an infectious disease caused by unicellular parasites of the genus *Plasmodium*, afflicting over 500 million people, and leading to over one million deaths per year almost all of which are caused by *Plasmodium falciparum*.^{1,2} This makes malaria one of the most deadly diseases in the world and therefore a reason for global alarm.² The infection begins via the bite of the female *Anopheles* mosquito carrying the unicellular parasite *P. falciparum*. The intraerythrocytic stage of the parasitic lifecycle includes development from an early ring stage to the trophozoite phase, where large amounts of malaria pigment (hemozoin) are produced, and finally to a schizont stage where the parasite replicates. During the trophozoite phase the parasite digests large quantities of hemoglobin releasing toxic free ferrous protoporphyrin IX (Fe(II)PPIX) and denatured globin.^{3,4} The Fe(II)PPIX is oxidized to Fe(III)PPIX and aggregates into an insoluble biomineral known as hemozoin (malaria pigment), which is spectroscopically identical to its synthetic analogue β -hematin.^{5,6} Hemozoin (Hz) is composed of an array of dimers linked together by reciprocal iron–carboxylate bonds to one of the propionate side chains of adjacent FePPIX groups.⁷ Under physiological conditions this pigment remains insoluble and undegraded.⁸

* To whom correspondence should be addressed. E-mail: bayden.wood@sci.monash.edu.au.

[†] Monash University.

[‡] University of Cape Town.

[§] La Trobe University.

^{||} Australian Synchrotron.

- (1) Greenwood, B.; Mutabingwa, T. *Nature* **2002**, *415*, 670–672.
- (2) Sachs, J.; Malaney, P. *Nature* **2002**, *415*, 680–685.
- (3) Schmitt, T. H.; Frezzatti, W. A., Jr.; Schreier, S. *Arch. Biochem. Biophys.* **1993**, *307*, 96–103.
- (4) Sugioaka, Y.; Suzuki, M. *Biochim. Biophys. Acta* **1991**, *1074*, 19–24.
- (5) Slater, A. F. G.; Swiggard, W. J.; Orton, B. R.; Flitter, W. D.; Goldberg, D. E.; Cerami, A.; Henderson, G. B. *Proc. Natl. Acad. Sci. U.S.A.* **1991**, *88*, 325–329.
- (6) Bohle, D. S.; Conklin, B. J.; Cox, D.; Madsen, S. K.; Paulson, S.; Stephens, P. W.; Yee, G. T. *Am. Chem. Soc. Symp. Ser.* **1994**, *572*, 497–515.
- (7) Pagola, S.; Stephens, P. W.; Bohle, D. S.; Kosar, A. D.; Madsen, S. K. *Nature* **2000**, *404*, 307–310.
- (8) Deegan, T.; Maegraith, B. G. *Ann. Trop. Med. Parasitol.* **1956**, *50*, 194–211.

The importance of lipids as catalysts for Hz formation is well documented.^{9–13} The rate of formation of β -hematin under physiological conditions is found to increase in the presence of mono-oleoylglycerol (MOG).⁹ Jackson et al.¹⁰ identified neutral lipid bodies composed of di- and triacylglycerols within the digestive vacuole (DV) of the parasite, which may represent storage compartments for lipid intermediates during phospholipid digestion. Hz formation in *Schistosoma mansoni* and *Rhodnius prolixus* occurs in lipid droplets and on the perimicrovillar membranes, respectively.¹¹ Egan et al.¹² have shown that the Hz analogue, β -hematin, under physiological conditions spontaneously forms at a lipid/water interface. In addition, Pisciotta et al.¹³ investigating the crystallization of FePPIX in *P. falciparum* have recently reported TEM (transmission electron microscopy) images of Hz formation in neutral lipid nanospheres at early (ring) and late (trophozoite) stages of the parasitic lifecycle within the DV. Given the importance of lipids in Hz formation, a spectroscopic method for the detection of lipid signatures in infected erythrocytes would seem an ideal approach to distinguish parasites at the early stages of intraerythrocytic development.

Several diagnostic techniques have been employed for malaria detection, these include fluorescence microscopy,^{14–18} polymerase chain reaction (PCR)-based assays,^{18–20} serological (dipstick) antigen detection,^{18,21–23} flow cytometry^{18,24} and laser desorption mass spectrometry.²⁵ Hitherto, the potential of vibrational spectroscopic techniques as malaria diagnostics have not been exploited, which is surprising given the important role the technique has played in understanding the molecular and electronic structure of β -hematin and Hz.^{4,6,26,27} In an early study by Slater et al.⁵ Fourier transform infrared (FT-IR) spectroscopy was used to identify vibrational modes specifically associated with the

propionate groups that link the heme groups together in the heme dimeric array.⁵ Initial resonance Raman studies by Ong et al.^{28,29} demonstrated the potential of Raman spectroscopy to detect Hz in fixed cells. With the use of resonance Raman spectroscopy, Wood et al.³⁰ observed dramatic band enhancement of specific vibrational modes of Hz using near-IR excitation wavelengths. This enhancement could be used to identify and image Hz within the DV of single infected functional erythrocytes.³¹ More recently the technique has been applied to investigate the interaction of chloroquine-based antimalarial drugs with Hz and β -hematin.^{32,33}

Although several resonance Raman studies have been applied to detect and monitor the formation of Hz in erythrocytes, hitherto the diagnostic potential of FT-IR spectroscopy has not been investigated. FT-IR has the advantage of being more sensitive to the lipid moieties than Raman spectroscopy thereby potentially enabling detection of parasites prior to Hz formation. In addition, the lipid bands are very weak when shorter excitation wavelength lasers are applied, and at high Raman excitation laser power it can photodegrade the cell. Furthermore, the time taken to perform a Raman map and produce spectra showing an acceptable signal-to-noise ratio (S/N) is approximately 10–30 min with a conventional Raman microscope as opposed to 1 min with a synchrotron FT-IR microscope. Moreover, to record a map of thousands of cells using a Raman microscope would take many hours compared to 1–3 min when using a conventional FT-IR imaging microscope with a focal plane array (FPA) detector.

Here, after preliminary experiments using FPA IR imaging to confirm the ability of IR analysis to observe Hz directly in infected red blood cells, we combine synchrotron FT-IR microspectroscopy with principal components analysis (PCA) to differentiate between the intraerythrocytic stages of the parasitic lifecycle based on the molecular signatures of Hz and specific lipid markers. To demonstrate the diagnostic utility of FT-IR spectroscopy we employed an artificial neural network (ANN) to unambiguously differentiate the different stages of the parasite. The results show a clear correlation between lipid signature and the stage of the intraerythrocytic development and demonstrate the diagnostic potential of combining FT-IR spectroscopy with neural networks as an independent modality to unequivocally identify parasites at different stages of the erythrocytic life cycle.

EXPERIMENTAL SECTION

Cell Culture. *P. falciparum* (D10 strain) was maintained in continuous culture using human erythrocytes from three different individuals obtained from the Red Cross Blood Bank, Melbourne.³⁴ Parasitized erythrocytes were cultured in complete

- (9) Fitch, C. D.; Cai, G.-z.; Chen, Y.-F.; Shoemaker, J. D. *Biochim. Biophys. Acta* **1999**, *1454*, 31–37.
- (10) Jackson, K. A.; Klonis, N.; Ferguson, D. J. P.; Adisa, A.; Dogovski, C.; Tilley, L. *Mol. Microbiol.* **2004**, *54*, 109–122.
- (11) Oliveira, M. F.; Kycia, S. W.; Gomez, A.; Kosar, A. J.; Bohle, D. S.; Hempelmann, E.; Menezes, D.; Vanier-Santos, M. A.; Oliveira, P. L.; Ferreira, S. T. *FEBS Lett.* **2005**, *579*, 6010–6016.
- (12) Egan, T. J.; Chen, J. Y.-J.; de Villiers, K. A.; Mabotha, T. E.; Naidoo, K. J.; Nookazi, K. K.; Langford, S. J.; McNaughton, D.; Pandiancherri, S.; Wood, B. R. *FEBS Lett.* **2006**, *580*, 5105–5110.
- (13) Pisciotta, J. M.; Coppens, I.; Tripathi, A. K.; Scholl, P. F.; Shuman, J.; Bajad, S.; Shulaev, V.; Sullivan, D. J., Jr. *Biochem. J.* **2007**, *402*, 197–204.
- (14) Richards, D. F.; Hunter, D. T.; Janis, B. *Am. J. Clin. Pathol.* **1969**, *51*, 280–283.
- (15) Sodeman, T. M. *Am. J. Trop. Med. Hyg.* **1970**, *19*, 40–42.
- (16) Shute, G. T.; Sodeman, T. M. *Bull. W.H.O.* **1973**, *48*, 591–596.
- (17) Makler, M. T.; Ries, L. K.; Ries, J.; Horton, R. J.; Hinrichs, D. J. *Am. J. Trop. Med. Hyg.* **1991**, *44*, 11–16.
- (18) Hanscheid, T. *Clin. Lab. Haematol.* **1999**, *21*, 235–245.
- (19) Humar, A.; Ohrt, C.; Harrington, M. A.; Pillai, D.; Kain, K. C. *Am. J. Trop. Med. Hyg.* **1997**, *56*, 44–48.
- (20) Humar, A.; Harrington, M. A.; Kain, K. C. *Trans. R. Soc. Trop. Med. Hyg.* **1997**, *91*, 406–409.
- (21) Makler, M. T.; Palmer, C. J.; Ager, A. L. *Ann. Trop. Med. Parasitol.* **1998**, *92*, 419–433.
- (22) Shiff, C. J.; Minjas, J. N.; Premji, Z. *Parasitol. Today* **1994**, *10*, 494–495.
- (23) Garcia, M.; Kirimoama, S.; Marlborough, D.; Leafasia, J.; Rieckmann, K. H. *Lancet* **1996**, *347*, 1549.
- (24) van Vianen, P. H.; van Engen, A.; Thaithong, S.; van der Keur, M.; Tanke, H. J.; van der Kaay, H. J.; Mons, B.; Janse, C. J. *Cytometry* **1996**, *14*, 276–280.
- (25) Demirev, P. A.; Feldman, A. B.; Kongkasuriyachai, D.; Scholl, P.; Sullivan, D. J., Jr.; Kumar, N. *Anal. Chem.* **2002**, *74*, 3262–3266.
- (26) Brémard, C.; Girerd, P.; Kowalewski, P.; Merlin, J. C.; Moreau, S. *Appl. Spectrosc.* **1993**, *47*, 1837–1842.
- (27) Wood, B. R.; McNaughton, D. *Expert Rev. Proteomics* **2006**, *3*, 525–544.

- (28) Ong, C. W.; Shen, Z. X.; Ang, K. K. H.; Kara, U. A. K.; Tang, J. *Appl. Spectrosc.* **2002**, *56*, 1126–1131.
- (29) Ong, C. W.; Shen, Z. X.; Ang, K. K. H.; Kara, U. A. K.; Tang, S. H. *Appl. Spectrosc.* **1999**, *53*, 1097–1101.
- (30) Wood, B. R.; Langford, S. J.; Cooke, B. M.; Lim, J.; Glenister, F. K.; Duriska, M.; Unthank, J. K.; McNaughton, D. *J. Am. Chem. Soc.* **2004**, *126*, 9233–9239.
- (31) Wood, B. R.; Tait, B.; McNaughton, D. *Appl. Spectrosc.* **2000**, *54*, 353–359.
- (32) Cintá-Pinzaru, S.; Peica, N.; Küstner, B.; Schlückner, S.; Schmitt, M.; Frosch, T.; Faber, J. H.; Bringmann, G.; Popp, J. *J. Raman Spectrosc.* **2006**, *37*, 326–334.
- (33) Frosch, T.; Küstner, B.; Schlückner, S.; Szeghalmi, A.; Schmitt, M.; Kiefer, W.; Popp, J. *J. Raman Spectrosc.* **2004**, *35*, 819–821.
- (34) Trager, W.; Jensen, J. B. *Science* **1976**, *193*, 673–675.

culture medium (CCM) consisting of RPMI 1640 (GIBCO-BRL), 25 mM hydroxypiperazine-*N'*-2-ethane sulfonic acid (HEPES, Sigma pH 7.4), 2 g/L sodium bicarbonate (AnalaR), and 4 mM Glutamax (Invitrogen). This was supplemented with 0.16% glucose (AnalR), 0.21 mM hypoxanthine (Sigma), 22 $\mu\text{g/mL}$ gentamicin (Sigma), 4% human serum, and 0.25% Albumax I (GIBCO-BRL). The cultures were incubated at 37 °C in a humidified atmosphere of 5% CO₂, 1% O₂, and 90% N₂. Infected red blood cells (RBCs) and uninfected RBCs (controls) were fixed in solution using 2% paraformaldehyde, 0.0075% glutaraldehyde, and 0.1 M cacodylate buffer for 1 h before being washed twice with Milli-Q water and placed on individual 12 mm diameter \times 0.5 mm thick CaF₂ IR grade polished windows. Excess water was removed, and the windows were allowed to dry. The experiment was repeated three times.

FT-IR Spectroscopy. FT-IR synchrotron measurements were performed on the FT-IR beamline at the Australian Synchrotron operating at 3 GeV and a maximum current of 200 mA. Spectra were collected with a Bruker Hyperion 2000 IR confocal microscope (Bruker Optics GmbH., Ettlingen, Germany) equipped with a liquid-nitrogen-cooled mercury–cadmium–telluride (MCT) detector with a 36 \times IR objective. The Hyperion 2000 microscope is coupled to a Bruker Vertex 80v spectrometer. Data collection was carried out using Bruker's proprietary OPUS version 6.5 software, with an additional 3D package (Bruker Optics GmbH., Ettlingen, Germany). The Hyperion microscope and sample was purged with dry nitrogen gas to minimize water vapor contributions in the spectra. For FT-IR mapping and line scans the rectangular aperture was set at 4 \times 4 μm^2 . A total of 128 sample scans per spectrum were collected from 30 individual cells for each erythrocytic stage in transmission mode by scanning the computer-controlled microscope stage to preselected points using the video-assisted software. Interferograms were collected double-sided at a resolution of 6 cm⁻¹ and Fourier transformed using a Blackman–Harris three-term apodization function with a zero-filling factor of 4.

FT-IR FPA measurements were performed on the Varian Stingray FT-IR microscope system (600 UMA) equipped with a liquid-nitrogen-cooled MCT 64 \times 64 pixel FPA detector with a 15 \times IR objective. The microscope is coupled to a Varian 7000 spectrometer. The microscope and FT-IR spectrometer were continually purged with nitrogen. Interferograms (128 coadded) were collected in transmission mode double-sided at a resolution of 6 cm⁻¹ and Fourier transformed using a Blackman–Harris four-term apodization function with a zero-filling factor of 4.

Attenuated total reflectance (ATR) FT-IR spectra of synthetic hemozoin (β -hematin) were recorded at a resolution of 6 cm⁻¹ using a Golden Gate diamond ATR (SPECAC, P/N10500 series) coupled to a Bruker IFS-55 FT-IR spectrometer (Bruker Optics GmbH., Ettlingen, Germany) using OPUS 6.0 spectroscopic software with an extended ATR correction algorithm and equipped with a liquid-nitrogen-cooled MCT detector where 50 scans were averaged.

Data Analysis. Each image from the FPA IR data contained approximately 1000 spectra of a large population of RBCs. Spectra with insufficient S/N or artifacts such as baseline effects and strong Mie scattering were removed from the data set, and the remaining spectra for each lifecycle stage were averaged to

produce high S/N ratio spectra with no baseline correction applied. Standard deviation spectra were also calculated and presented.

Initial spectral manipulations on the synchrotron data were carried out under OPUS. Each sample data set contained 30 spectra, which were averaged independently to produce the mean spectra presented. Second-derivative FT-IR spectra were calculated using the Savitzky–Golay algorithm with 13 smoothing points. Although using second derivatives reduces spectral resolution and precludes the use of spectral intensities in analysis we used it here to allow for easier visualization of spectral change and to minimize the effects of baseline variation in the spectral database. N.B. in the second derivative spectra the absorbance maxima become minima and in the discussion below intensities are thus +ve for absorbance spectra and –ve for second-derivative spectra. Difference spectra were calculated directly from vector-normalized raw spectra in absorbance mode and then converted to second derivatives. The converted spectra enable easier visualization of bands within a broad background of multicomponent absorption bands and minimized the effects of Mie scattering.

Principal Components Analysis. In this study, PCA was applied to investigate the spectra of parasites at different stages of the intraerythrocytic life cycle. PCA reduces the dimensionality of a data set by decomposing the data set into a signal and noise part. The objects (spectra) are plotted onto principal components (PCs). Each consecutive PC is orthogonal with respect to the previous and each accounts for a decreasing proportion of the variance. The scores and loadings plots are used to analyze the data when a PCA model is decomposed. A plot of the scores allows similarities and differences in the data to be visualized. Each point in the scores plot represents a single spectrum on a two-dimensional axis. The individual variance calculated for each spectrum contributes to the position of each score on a given PC.³⁵ The loadings plot is then used in combination with the scores plot to identify the variables (wavenumber values) that contribute to the variability in the data set. PCA was performed on second-derivative spectra after an extended multiplicative scatter correction (EMSC) was applied to the data.³⁶ PCA was applied to data sets from a control and three test samples: rings, trophozoites, and schizonts. A spectral window between 1800 and 1000 cm⁻¹ was used to examine Hz bands and compare the control and the trophozoite groups. Spectral windows of 3100–2800 cm⁻¹ were also used to examine lipid bands and compare the control group to each of the three life cycle stages of the parasite. PCA was also performed on all data sets at once (control, rings, trophozoites, and schizonts) using this spectral range. All data were mean-centered, and a full cross validation PCA was performed using the Unscrambler (V9.0 CAMO, Norway) software package.

Artificial Neural Network Classification. ANN analysis was performed using the NeuroDeveloper 2.5b 2004 SynthonSoftware. All the networks were trained to solve a four-class classification problem to test for identification of three classes of infection: ring, trophozoite, and schizonts versus controls from three patients. The available spectra (data set) were split into three subsets: a

(35) Solomonov, I.; Osipova, M.; Feldman, Y.; Baecht, C.; Kjaer, K.; Robinson, I. K.; Webster, G. T.; McNaughton, D.; Wood, B. R.; Weissbuch, I.; Leiserowitz, L. *J. Am. Chem. Soc.* **2007**, *129*, 2615–2627.

(36) Martens, H.; Starks, E. *J. Pharm. Biomed. Anal.* **1991**, *9*, 625–635.

training set (54%), a validation set (13%), and a test set (33%). Network layout was optimized by testing varying numbers of neurons in the hidden layer for the lowest training and validation data set errors. The number of available sample spectra was limited, and hence, it was necessary (to ensure good theoretical generalization)^{37,38} to compress the input spectra with a covariance-based feature selection algorithm. The ANN analysis was performed on second-derivative spectra derived from the raw spectra and processed using a Savitzky–Golay algorithm with 13 smoothing points and then vector-normalized.

ANN analysis was performed on different spectral windows to investigate which bands within the spectra contained the most important information for distinguishing infected cells from uninfected cells. The spectral windows used were (1) 3100–2800 and 1800–1000 cm^{-1} , (2) 3100–2800 cm^{-1} , and (3) 1800–1000 cm^{-1} . In this manner, it was possible to explore the effect on ANN prediction accuracy by leaving out spectral regions associated with the least variability between classes. For each optimized network, the prediction accuracy was determined from classifications performed on the test set. Classification accuracy of an ANN's performance was calculated as the number of correctly classified spectra divided by the total number of test spectra expressed as a percentage. Sensitivity and specificity binary classification measures were calculated where an ANN classification of infected cells (regardless of parasite stage) was taken as a positive test result.

Materials and Synthesis. β -Hematin was prepared as described by Egan et al.³⁹ by dissolving hemin (Fluka, Biochemika) in 3 mL of 0.1 M NaOH and stirring. To the solution was added 0.3 mL of 0.1 M HCl and 1.74 mL of 12.9 M acetate (pH 5). The reaction was complete after 30 min at 60 °C after which the mixture was cooled for 10 min on ice and then filtered.³⁹ The resultant solid was dried for 24 h at 37 °C.

RESULTS AND DISCUSSION

Red blood cells make ideal subjects for FT-IR synchrotron spectroscopy because they are anucleated and the microscope aperture ($4 \times 4 \mu\text{m}^2$) is less than the diameter of the cell ($\sim 8 \times 8 \mu\text{m}^2$); hence, Mie scattering from cell nuclei and dispersion from edge effects that is normally associated with eukaryotic cells is minimized. A synchrotron FT-IR vector-normalized mean spectrum of RBCs (control) and a typical spectrum of a single erythrocyte infected with the *P. falciparum* parasite (trophozoite-infected) are displayed in Figure 1. The most prominent features observed in the spectra are strong broad bands at 1656 and 1542 cm^{-1} assigned to the C=O stretching vibration of proteins coupled to NH_2 in-plane bending vibrations (amide I), with contributions from C=O stretching modes of DNA nucleotides.^{31,40–44} The 1542 cm^{-1} band is also from cell

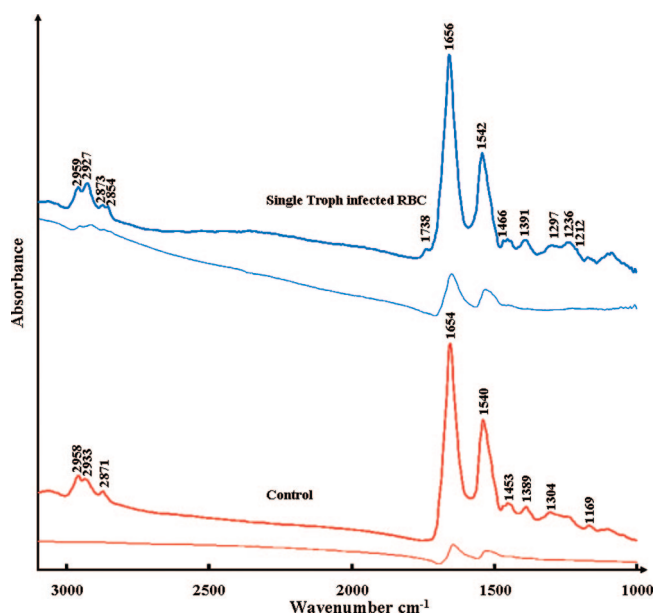


Figure 1. Synchrotron FT-IR vector-normalized spectra of averaged RBCs (control) and a single RBC infected with the *P. falciparum* parasite (trophozoite stage). Standard deviation spectra are shown below each spectrum.

proteins typically from N–H bending coupled to a C–N stretching mode (amide II) and also nucleic acid conformational markers ~ 1530 – 1330 cm^{-1} as previously described.^{31,45,46} The ester carbonyl band at $\sim 1738 \text{ cm}^{-1}$ from lipid moieties is more pronounced in the trophozoite-infected cell. Features attributable to Hz are not immediately obvious in the raw spectra of trophozoite-infected cells; consequently a difference spectrum between the control and the trophozoite spectrum was calculated and is shown in second-derivative form in Figure 2a. Bands are assigned by correlating the minima peaks in the second-derivative difference spectrum to the minima peaks in the second-derivative β -hematin spectrum (Figure 2b). Bands at 1713, 1664, and 1209 cm^{-1} correlate with Hz bands due to the H-bonded carboxylate group, the C=O, and the C–O stretching vibration of the propionate linkage, respectively.^{5,30} However, the C=O band from the Hz propionate band is partly obscured by an amide I feature due to protein differences in the two samples and thus appears as a shoulder feature of the amide I mode, while the C–O stretching vibration at 1209 cm^{-1} is very weak in the difference spectrum (Figure 2a). Given that Hz deposits are of the order of $1 \mu\text{m}$ compared with the $4 \mu\text{m}^2$ aperture, it is not surprising that these bands appear weak in the difference spectrum. However, these bands prove that Hz can be detected at the single-cell level. The single-cell difference spectrum below 1000 cm^{-1} is noisy because the $4 \times 4 \mu\text{m}^2$ aperture results in diffraction limited energy throughput.⁴⁷ The sensitivity is further reduced because of the transmission efficiency of the CaF_2 windows, which decreases dramatically below 1000 cm^{-1} . Here lies the intrinsic value of using the brightness of synchrotron light to analyze RBCs. The synchrotron light source is at least 100 times

(37) Despagne, F.; Massart, D. L. *Analyst* **1998**, *123*, 157R–178R.

(38) Hush, D. R.; Horne, B. G. *IEEE Signal Process. Mag.* **1993**, *1*, 8–39.

(39) Egan, T. J.; Ross, D. C.; Adams, P. A. *FEBS Lett.* **1994**, *352*, 54–57.

(40) Parker, F. S. *Application of Infrared Spectroscopy in Biochemistry, Biology and Medicine*; Plenum: New York, 1971.

(41) Miyazawa, T.; Shimanouchi, T.; Mizushima, S. *J. Chem. Phys.* **1956**, *24*, 408–418.

(42) Miyazawa, T.; Shimanouchi, T.; Mizushima, S. *J. Chem. Phys.* **1958**, *29*, 611–616.

(43) Susi, H., Ed. *Structure and Stability of Biological Macromolecules*; Marcel Dekker: New York, 1969.

(44) Surewicz, W. K.; Mantsch, H. H. *Biochim. Biophys. Acta* **1988**, *952*, 115–130.

(45) Benedetti, E.; Bramanti, E.; Papineschi, F.; Rossi, I.; Benedetti, E. *Appl. Spectrosc.* **1997**, *51*, 792–797.

(46) Susi, H.; Ard, J. S. *Spectrochim. Acta* **1971**, *27A*, 1549–1562.

(47) Carr, G. L. *Rev. Sci. Instrum.* **2001**, *72*, 1613–1619.

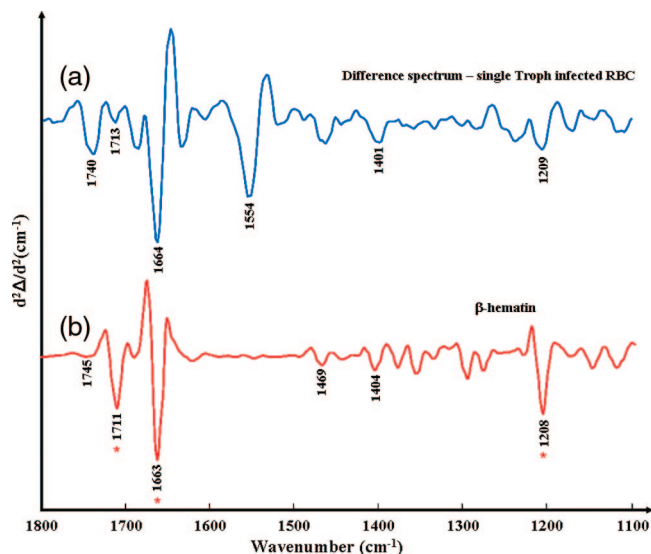


Figure 2. (a) Synchrotron FT-IR difference spectrum (trophozoite RBC – control RBC) shown as a second-derivative spectrum. (b) ATR/FT-IR second-derivative spectrum of β -hematin. (Asterisks indicates the hemozoin marker bands).

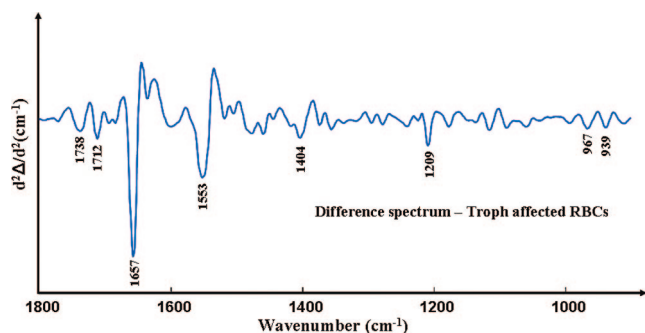


Figure 3. Focal plane array-FT-IR difference spectrum calculated from the average second-derivative spectra of trophozoite stage RBC minus average second-derivative spectra of control RBC.

brighter than a conventional global source, and this, in combination with the confocal nature of the FT-IR microscope, makes it possible to record spectra with a small $4 \times 4 \mu\text{m}^2$ aperture.

The carbonyl band associated with the propionate linkage is observed at 1664 cm^{-1} in the difference spectrum (Figure 2a), which is slightly shifted from its expected literature value of 1662 cm^{-1} .^{5,30} The apparent shift is the result of this band being superimposed on the amide I mode. The carbonyl band appears as a shoulder feature on the amide I band in the unprocessed spectrum with the center of this band obscured by the amide I mode. On calculating the difference spectrum the shoulder feature manifests as a band slightly blue-shifted compared to the literature value for isolated Hz. To further investigate these changes an FPA-FT-IR difference spectrum was calculated by subtracting the average trophozoite-affected cells from the average noninfected control (Figure 3). Although it is possible to record spectra of a cluster of cells using a conventional FPA-FT-IR microscope in rapid time and obtain a difference spectrum from uninfected and infected RBCs, it is not possible to resolve spectroscopic detail at the single-cell level with this approach. Bands observed at 1712 and 1209 cm^{-1} are assigned to the H-bonded carboxylate group and C–O stretching vibrations of the propionate linkage from

the Hz crystal, respectively.^{5,30} A strong feature where the C=O stretching vibrational band of the propionate linkage of Hz is expected supports this assignment, although this region is also affected by protein spectral changes as described below. The FPA enables thousands of FT-IR spectra to be collected simultaneously from a large sample area, and thus the S/N is improved upon averaging. The resulting difference spectrum clearly delineates the major Hz bands, including the 1209 cm^{-1} band, thus confirming the presence of Hz. The absence of the 1662 cm^{-1} band from Hz is due to the superposition of the amide I band from infected cells. Upon spectral subtraction with the control, a band appears at 1657 cm^{-1} , which is slightly shifted from the uninfected control which appears at 1654 cm^{-1} possibly indicative of denatured hemoglobin. The FPA has the advantage of rapid measurement time and ready accessibility without having to resort to a synchrotron source. However, it is not possible to obtain spectra of individual infected cells with the FPA because of the inherent limitations of a global source and numerical aperture of the Cassegrain objective; thus, a spatial resolution closer to $12\text{--}15 \mu\text{m}$ is achieved rather than the $5.5 \mu\text{m}$ that might be expected from the pixel size. With the improvement of global sources and microscope optics it may be possible to achieve single-cell spatial resolution using an FPA in the near future.

PCA analysis was applied to synchrotron FT-IR second-derivative spectra from control and *P. falciparum*-infected cells to assess spectral covariance across a subpopulation of cells. Figure 4A shows a clear separation in the scores plot of controls (O) and trophozoite (T)-infected cells along PC1, while Figure 4B shows the loadings plot for PC1. The PCA loadings plot (Figure 4B) displays strong negative loadings associated with vibrational modes of Hz located at 1712 and 1211 cm^{-1} . The ester carbonyl band from lipid moieties is also a strong negative loading at 1740 cm^{-1} . Strong positive loadings from the vibrational modes of amide I (1650 cm^{-1}) and amide II (1537 cm^{-1}) of proteins from hemoglobin are also strong contributors to the separation along PC1 in the scores plot (Figure 4A). The strong positive and negative loadings for both amide I and amide II are characteristic of different protein types and concentrations between the controls and infected cells. The explained variance for PC1 is 51% followed by 10% for PC2. The loadings plot is similar in appearance to the difference spectrum (Figure 3) calculated by subtracting the average control spectrum from the average trophozoite-infected RBC spectrum. Figure 5 depicts synchrotron FT-IR average baseline-corrected raw spectra from 30 single RBCs infected at various stages of the *P. falciparum* parasite's life cycle including the early ring stage, trophozoite, and schizont stages and for comparison the spectrum of uninfected (control) cells. The spectra, which are vector-normalized between the 3100 and 1000 cm^{-1} spectral range, show distinct and reproducible changes between the different stages. These include an increase in the bands at 2930 , 2852 , and 1741 cm^{-1} as the parasite matures. These bands are assigned to $\nu_{\text{asym}}(\text{CH}_2 \text{ acyl chain lipids})$, $\nu_{\text{sym}}(\text{CH}_2 \text{ acyl chain lipids})$, and ester carbonyl stretching vibrations, respectively. This is correlated with an increase in the ester carbonyl band at $\sim 1741 \text{ cm}^{-1}$ indicating the changes observed in the C–H stretching region are indeed from lipids. It has previously been hypothesized that as the

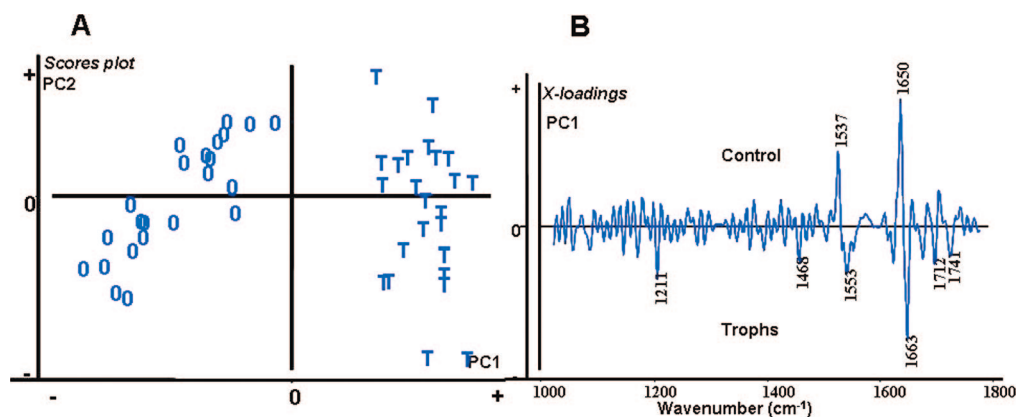


Figure 4. (A) PCA scores plot along PC1 and PC2 of control (0) and trophozoite affected RBC (T) data sets. (B) PCA loadings plot along PC1 of control group and trophozoite-affected cells taken from the PCA scores plot (Figure 3) after a second-derivative function was applied.

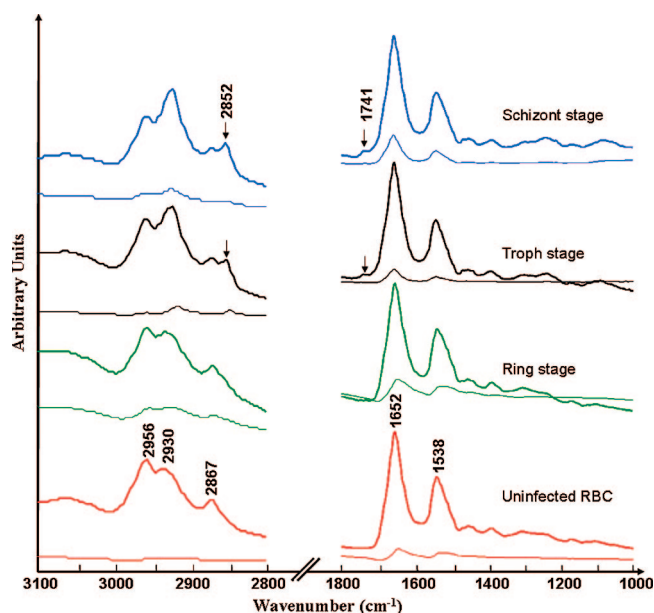


Figure 5. FT-IR averaged normalized spectra of the C–H stretching region and fingerprint region from the Australian Synchrotron of RBCs (control) and the three stages of the parasitic lifecycle (ring, trophozoite, and schizont) within a fixed RBC. Standard deviation spectra are shown below each spectrum for both spectral regions.

parasite matures and digests hemoglobin, the heme biomineral formed in its DV is engulfed in a lipid nanosphere.¹³ As the heme crystal grows within the lipid nanosphere¹³ longer chain fatty acids are thought to surround the growing crystal. Figure 6 shows the second-derivative spectra of the C–H stretching region from lipids in the DV of infected RBCs at different stages of the *P. falciparum* parasite intraerythrocytic cycle. The features in this spectral range for the control spectrum include weak bands at 3057 and 3027 cm⁻¹. These bands are assigned to aromatic C–H stretching vibrations of monosubstituted benzenes from amino acid side chains present in hemoglobin.^{48,49} In addition, the bands at 2957, 2926, and 2867 cm⁻¹ are from $\nu_{\text{asym}}(\text{CH}_3)$, $\nu_{\text{asym}}(\text{CH}_2)$, and $\nu_{\text{sym}}(\text{CH}_3)$ vibrational modes of amino acid side

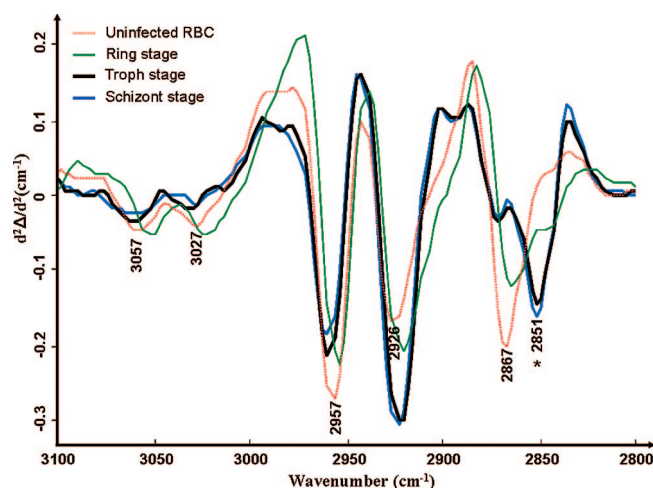


Figure 6. Average second-derivative spectra for infected RBCs (ring, trophozoite, and schizont stage parasites) and uninfected RBCs (control) of the C–H stretching region. (The asterisk indicates the appearance of a lipid band.)

chains, respectively.³¹ There is an apparent change in the ratio (or peak position) between the 2867 and 2851 cm⁻¹ band in the spectrum (Figure 6) of the ring stage parasites compared to the later stages. From a purely spectroscopic viewpoint, it is tempting to ascribe this change in peak position to be from an increase in concentration of branching in the aliphatic fatty acid side chain and a change in the lipid environment. However, the differences in peak position in the second-derivative spectra are more likely due to the change in slope of the spectral curve; hence, the peak intensities vary based on bandwidth of the raw spectra rather than concentration. Pisciotta et al.¹³ have previously demonstrated a lipid association with Hz formation through the use of TEM as part of a broader study to investigate the crystallization of heme in infected erythrocytes. The images at the early stage of the parasite's lifecycle show small heme crystals surrounded by neutral lipid spheres inside the DV compared to a thinner rim of lipids that surrounded a much larger heme crystal at the later trophozoite stage.¹³ Fitch et al.⁹ showed that unsaturated monoacylglycerols incubated with hematin are the most effective promoters of FePIX polymerization, whereas saturated lipids are incapable of promoting β -hematin crystal growth in vitro.

(48) Ramaswamy, S.; Rajaram, R. K.; Ramakrishnan, V. J. *Raman Spectrosc.* **2002**, *33*, 689–698.

(49) Cao, X.; Fischer, G. J. *Mol. Struct.* **2000**, *519*, 153–163.

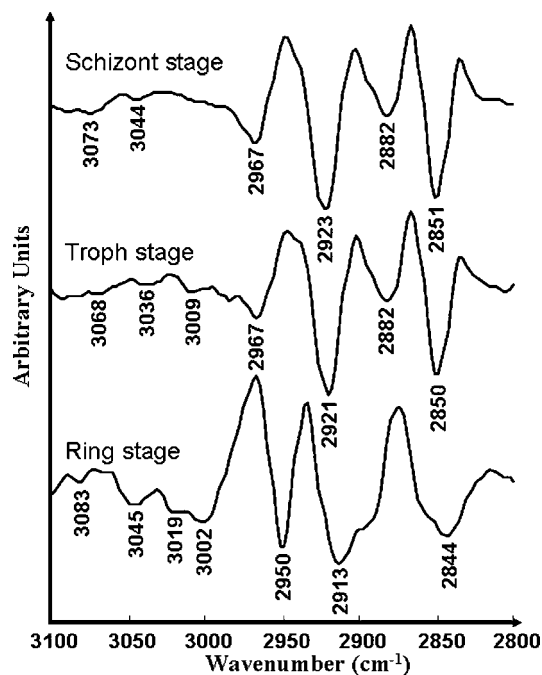


Figure 7. Difference spectrum of the average second-derivative spectra for infected RBCs (ring, trophozoite, and schizont stage parasites) minus average second-derivative spectra of uninfected RBCs (control).

Counter to this finding, electrospray ionization tandem mass spectrometry (ESI-MS/MS) identified the saturated lipids monostearic glycerol (MSG) and monopalmitic glycerol (MPG) present in the parasite's DV, which when combined associate with H_z at a ratio of approximately 2:1.¹³ In addition, Jackson et al.¹⁰ present lipid analysis data that indicate di- and triacylglycerols make up these neutral lipid spheres. They hypothesized that these spheres are storage compartments for lipid intermediates during phospholipid digestion in the parasite's DV.¹⁰ Figure 7 shows the difference spectrum for each stage of the parasite's lifecycle calculated within the C–H spectral range (3100–2800 cm^{−1}) from the average spectra presented in Figure 6. The features in the difference spectra (Figure 7) show a number of bands associated with a change in the type of unsaturated fatty acids and the formation of saturated fatty acid chains within the DV of the maturing parasite. The ring stage spectrum shows bands at 3002 and 3019 cm^{−1} associated with *cis* unsaturated fatty acids. There are also bands at 3036 and 3068 cm^{−1}. From a purely spectroscopic viewpoint it is tempting to assign these bands to *trans* fatty acids based on lipid model compounds;^{50–53} however, to date there is no evidence for *trans* fatty acids in *P. falciparum*. Ferreri et al.⁵⁴ have recently shown that radical chemistry can lead to the formation of *trans* fatty acids; however, this is not likely the case here. These difference band features are more likely to be due to changes in the aromatic C–H

stretching vibrations of the amino acid side chains through digestion of Hb by the parasite. The difference spectrum of the schizont stage shows no evidence of bands associated with a *cis* conformation of unsaturated lipids and therefore suggests an increase in saturated fatty acids. The methyl and methylene C–H band shifts and an increase in its intensity suggests that the lipid environment surrounding the H_z crystal changes significantly. These changes could be accounted for by a change in the length of fatty acid side chains present in the lipid as the parasite matures.

Figure 8a shows a scores plot based on a PCA performed on all intraerythrocytic stages and the control collectively from decomposing the C–H (3100–2800 cm^{−1}) stretching region. The scores plot shows a separation mainly along PC1 between the three different stages with the schizonts (S) separating furthest away from the control group, followed by the trophozoites (T) and then the rings (R), which in turn cluster very close to the controls with some degree of separation along PC2. The explained variance for PC1 is 68% and 6% for PC2. The loadings plot in Figure 8b displays strong negative loadings, which indicate the variance along PC1 in the infected cells is due to a change in lipid concentration or composition. These changes are evident in the 2921 and 2851 cm^{−1} bands associated with the asymmetric and symmetric methylene C–H stretches from acyl chain lipids. Figure 8c shows strong positive loadings along PC2 at 2962, 2931, 2874, and 2856 cm^{−1}, which are associated with bands from the lipid environment surrounding the H_z crystal. However, these bands have little significance in the separation of infected cells due to the low explained variance of PC2.

Table 1 shows sensitivity and specificity measures for the detection of parasite infection obtained from three ANNs trained on the three different spectral windows. The C–H and fingerprint regions selected together gave the highest sensitivity and specificity. Table 2 shows classification accuracy of all infected stages compared to control. The combined C–H and fingerprint regions produced the highest accuracy with 100% accuracy being achieved for all three infected stages. The ANN was able to classify rings from controls, whereas PCA was unable to clearly separate the two groups on the scores plot observed in Figure 8a. Presumably, the ANN models out performed the PCA because unlike PCA, ANNs are able to exploit nonlinear relations within the data set.

An early study by Slater et al.⁵ presented the first FT-IR spectrum of H_z using a conventional FT-IR spectrometer. After sonication of *P. falciparum*-infected RBCs and purification of the resultant H_z pellet the FT-IR spectrum of the H_z was found to be spectroscopically identical to its synthetic analogue β -hematin. Furthermore Wood et al.⁵⁵ have previously spectroscopically detected H_z in live parasites using near-IR resonance Raman spectroscopy and compared this with the Raman spectrum of β -hematin. Although this last study showed the presence of H_z in infected erythrocytes using Raman spectroscopy, no study has yet shown the presence of H_z in infected RBCs using FT-IR spectroscopy. We have demonstrated that synchrotron FT-IR spectroscopy in combination with multivariate methods can detect the presence of H_z in single infected RBCs. The technique can also be used to differentiate between the three stages of the parasitic lifecycle based on fatty acid composition within the DV

(50) Shukla, N.; Svedberg, E. B.; Ell, J. *Colloids Surf., A* **2007**, *301*, 113–116.

(51) Sinclair, R. G.; McKay, A. F.; Myers, G. S.; Jones, R. N. *J. Am. Chem. Soc.* **1952**, *74*, 2578–2585.

(52) Lee, D. H.; Condrate, R.; Lacourse, W. C. *J. Mater. Sci.* **2000**, *35*, 4961–4970.

(53) Vogel-Weill, C.; Gruger, A. *Spectrochim. Acta., Part A* **1996**, *52*, 1737–1755.

(54) Ferreri, C.; Panagiotaki, M.; Chatgililoglu, C. *Mol. Biotechnol.* **2007**, *37*, 19–25.

(55) Wood, B. R.; Langford, S. J.; Cooke, B. M.; Glenister, F. K.; Lim, J.; McNaughton, D. *FEBS Lett.* **2003**, *554*, 247–252.

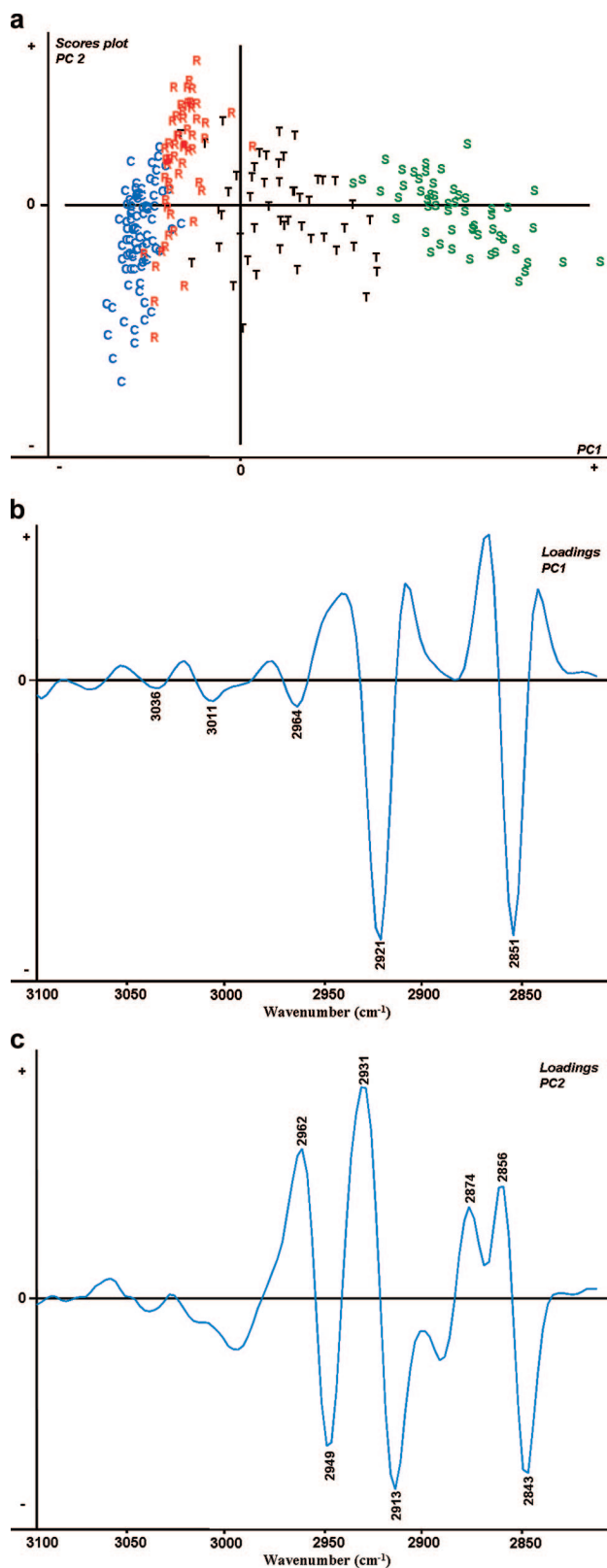


Figure 8. (a) PCA scores plot of the C–H stretching region along PC1 and PC2 of control (C) and all three stages of infection (ring (R), trophozoite (T), and schizont (S)) with RBCs. (b) PCA loadings plot of the C–H stretching region along PC1 of control (C) and all three stages of infection (ring, trophozoite, and schizont) within RBCs after a second-derivative function was applied. (c) PCA loadings plot of the C–H stretching region along PC2 of control (C) and all three stages of infection (ring, trophozoite, and schizont) within RBCs after a second-derivative function was applied.

Table 1. Artificial Neural Network (ANN) Sensitivities and Specificities of Infected and Uninfected RBCs for the Three Spectral Ranges Trialed

spectral range (cm ⁻¹)	3100–2800, 1800–1000	3100–2800	1800–1000
sensitivity (%)	100	93	99
specificity (%)	92	88	91

Table 2. Artificial Neural Network (ANN) Accuracies for Correctly Classifying Control, Rings, Trophozoites, and Schizonts for the Three Spectral Ranges Trialed

spectral range (cm ⁻¹)	3100–2800, 1800–1000	3100–2800	1800–1000
control	92	88	91
rings	100	79	96
trophozoites	100	96	100
schizonts	100	92	100

of infected erythrocytes. This provides a fundamental insight into the biochemistry of lipid within the maturing parasite. It shows that besides the morphological differences observed between the intraerythrocytic life cycle stages of the parasite there are specific changes in lipid composition that give rise to a very specific lipid signature in the 3100–2800 cm⁻¹ region of the mid-IR spectrum.

Bright-field microscopy has been the standard for malaria diagnosis since the discovery of the disease in 1880. The technique has a number of advantages, the main one being the ability to quantify and identify the parasites at different stages of the parasite's life cycle. With this information it is possible to work out a treatment regime specific for the patient. However, microscopy also has several disadvantages, the major one being that it is subjective and requires experienced personnel to make the diagnosis. Rapid diagnostic tests (RDTs) also known as “dipsticks”, provide an alternative to microscopy. RDTs make use of a capture antibody and conjugated detection antibody to detect malarial antigen in blood samples. The advantages of this approach include the rapid turnaround time and the simplicity of use, which allow clinicians to make on-the-spot diagnoses. However, quantification of infected parasites with RDTs is not possible at this time, which is important as knowledge of the parasite number often determines the therapeutic approach. Although the sensitivity is good (40 parasites/μL of blood), the cost of dipsticks has limited their use in the developing world where these tests are needed. Laser desorption mass spectrometry (LD-MS) is able to detect H₂ to a sensitivity of 100–1000 parasites/μL of blood, roughly similar to routine microscopy. However, the technique relies on the presence of H₂, and therefore early ring stages of the parasite would elude detection with this approach. Raman microscopy also shows potential as a diagnostic for malaria. However, like LD-MS it currently relies on the detection of H₂ in the cells, and consequently at present the technique has only been shown to detect later stages of the parasites life cycle.

Finding inexpensive, sensitive, and rapid methods for malaria diagnosis, which require minimal training for the technician, would have a major impact on malaria management. In this context FT-IR spectroscopy may offer several advantages compared to these other techniques in the foreseeable future. These include (1) the ability to detect all stages of the parasite's life cycle including the early ring stage prior to H₂ formation, (2) unambiguous nonsub-

jective diagnosis based on neural network spectral pattern recognition, (3) although the instrumentation is currently expensive the actual cost per test is very cheap especially if one uses inexpensive IR substrates such as Kevley slides, and (4) the technique has a sensitivity of 1 parasite/ μL of blood on a thin film when using a synchrotron source.

Of course a synchrotron source is not suited for a clinical environment, but with the continued development of confocal micro-FT-IR imaging spectrometers with powerful global sources, improved sensitivity FPA detectors, and new advances in computational algorithms for diagnosis, one can envisage FT-IR spectroscopy becoming a new weapon in the fight against malaria. These results lay the foundation for the future development of an IR-based technology that would be rapid, nonsubjective, and may one day not be dependent on the brightness of a synchrotron source to obtain the required spatial resolution for high-performance single-cell spectroscopy.

ACKNOWLEDGMENT

This work is supported by an Australian Research Council Discovery Grant. Dr. Bayden Wood was supported by an Australian Synchrotron Research Fellow Grant and a Monash Synchrotron Research Fellowship. We thank the IR beamline scientist Dr. Ljiljana Puskar from the Australian Synchrotron for FT-IR beamtime and experimental support. Katherine de Villiers was supported by an Equity Development Program scholarship of the Department of Chemistry, University of Cape Town. Support (Timothy Egan and Katherine de Villiers) also came from the National Research Foundation under Grant No. 2061833 and the Medical Research Council of South Africa.

Received for review October 31, 2008. Accepted February 9, 2009.

AC802291A